CrystEngComm

ROYAL SOCIETY OF CHEMISTRY

PAPER

View Article Online
View Journal | View Issue



Cite this: *CrystEngComm*, 2026, **28**, 3259

# Structure and luminescence colour change of an iridium(III) bis-terpyridine complex crystal triggered by water sorption/desorption

Yusuke Endo,[a] Mio Kondo,[a] Tomoe Nakamura,[a] Shingo Hattori,[a] Akiko Sekine,[b] Sosuke Kojo[b] and Kazuteru Shinozaki *[a]

A cationic complex crystal of $[Ir(tpy)_2]Br_3{\cdot}7H_2O$ (tpy = 2,2′:6′,2″-terpyridine) shows luminescence vapochromism as a reversible conversion between yellow and orange emissions in response to heating/cooling. X-ray crystallography reveals that $[Ir(tpy)_2]Br_3{\cdot}7H_2O$ exists as a triclinic crystal system, comprising Ir(III) complex layers and 2D hydrophilic sheets of $H_2O$ and $Br^-$. The orange emissive crystal is determined to be the orthorhombic $[Ir(tpy)_2]Br_3{\cdot}2H_2O$, comprising 1D hydrophilic channels of $H_2O$ and $Br^-$, with $Br^-$ in close proximity to the Ir(III) complex. The yellow emission of $[Ir(tpy)_2]Br_3{\cdot}7H_2O$ is due to the dual emission from the ligand-centered π–π* transition and the $Br^-$-to-ligand charge transfer (XLCT). The π–π* emission is quenched by the switching to the XLCT emission by the close approach of $Br^-$ to Ir(III) complex resulting from the $H_2O$ desorption. The reversible $H_2O$ sorption/desorption results in not only the luminescence colour change but also the drastic structural change between triclinic and orthorhombic crystal systems. The weak stimulus of $H_2O$ sorption/desorption triggers the phase transition of the Ir(III) complex crystal; 5 $H_2O$ molecules are incorporated into the 1D channel of the $[Ir(tpy)_2]Br_3{\cdot}2H_2O$ crystal to change the Ir–$Br^-$ framework from orthorhombic to triclinic, and inversely, the elimination of 5 $H_2O$ molecules from the 2D hydrophilic sheet in $[Ir(tpy)_2]Br_3{\cdot}7H_2O$ contributes to the reconstruction of the hydrophilic channel along with the reversion of the framework to orthorhombic.

Received 10th March 2026,
Accepted 20th April 2026

DOI: 10.1039/d6ce00194g

rsc.li/crystengcomm



## Introduction

Most crystals consisting of transition metal complexes do not lose their crystallinity and intrinsic colour even when cracked and ground into fine powders because their periodic alignments of components remain the same. However, some Pt(II) complexes frequently show the loss of crystallinity resulting from amorphization upon mechanical grinding, thereby changing their colour and luminescence. For example, Pt(5mdpb)Cl (5mdpbH = 1,3-di(5-methyl-2-pyridyl)benzene)[1] and Pt(5fdpb)Cl (5fdpbH = 1,3-di(5-trifluoromethyl-2-pyridyl)benzene)[2] crystals show the colour change from yellow to orange with the switching of the excited state from the π–π* state to the MMLCT (metal metal-to-ligand charge transfer) state of the Pt–Pt dimeric form. Thereafter, reports on the MMLCT emission of Pt(II) complex crystals based on the mechanochromism increased.[3–11] Occasionally, such a weak mechanical stimulus causes not only the dimerization of the ground Pt(II) complex but also the excimer formation of the Pt(II) complex;[12–17] a Pt(5mdpb)Cl (5mdpbH = 1,3-di(5-methyl-2-pyridyl)benzene) crystal[1] shows no change in the crystal structure and colour even upon mechanical grinding, but it emits an orange luminescence different from the original yellow emission before grinding. The orange luminescence is attributed to the (Pt–Pt)* excimer formation on the surface of the powdered crystals.

Exposure to solvent vapor, which is another weak external stimulus, also induces a colour change in the Pt(II) complex crystal.[18–20] For instance, a purple crystal of Pt(Fmdpb)CN (FmdpbH = 4,6-difuluoro-1,3-di(5-methyl-2-pyridyl)benzene), showing no visible luminescence, suddenly emits a red luminescence along with a red colouration upon exposure to chloroform vapor.[21] The characteristic colour change is attributed to the emergence of visible absorption due to the MMLCT transition in the dimeric $[Pt(Fmdpb)CN]_2$ moiety upon sorption of $CHCl_3$ vapor into the crystal. These neutral and planar Pt(N^C^N) complex crystals, exhibiting a colour change in response to mechanical grinding or exposure to $CHCl_3$ vapor, are classified as "soft crystals",[22,23] one of the categories of smart materials, which can easily change their structure by weak stimulus while retaining their highly ordered structures. So far, many materials consisting of neutral compounds, including organic molecules, organometallic complexes, and

[a] *Graduate School of Nanobioscience, Yokohama City University, 22-2 Seto, Kanazawa-ku, Yokohama 236-0027, Japan. E-mail: shino@yokohama-cu.ac.jp*
[b] *School of Science, Institute of Science Tokyo, 2-12-1 O-okayama, Meguro-ku, Tokyo 152-8551, Japan*

transition metal complexes, have been found to show the characteristics of "soft crystals", which is the change in morphology, colour, or luminescence as a response to weak external stimulus such as mechanical stress, exposure to vapor, or heating.[24] Recently, we presented vapochromic characteristics of a cationic complex salt, $[Ir(tpy)_2]I_3{\cdot}2H_2O$ (tpy = 2,2′:6′,2″-terpyridine), for which colour switches between orange and red during the sorption/desorption of $H_2O$ from/to the atmosphere.[24] Reports on luminescence vapochromism of Ir(III) complexes seem to be limited compared to Pt(II) complexes.[25–31]

The strong visible colouration is due to the $I^-$-to-tpy ligand charge transfer (XLCT) transition of $[Ir(tpy)_2]I_3{\cdot}2H_2O$,[32] where the HOMO, a 5p orbital of $I^-$, is strongly influenced by the number of hydrated $H_2O$ molecules, resulting in the shift of the XLCT band. The X-ray crystallography of $[Ir(tpy)_2]I_3{\cdot}2H_2O$ revealed that $H_2O$ molecules are stored in hydrophilic channels and connected with $I^-$ by hydrogen bonds. A Rietveld analysis of the PXRD patterns for $[Ir(tpy)_2]I_3{\cdot}nH_2O$ ($n$ = 0–2) clarified that the $[Ir(tpy)_2]I_3$ moieties construct a rigid framework and retain the original packing structure during the $H_2O$ sorption/desorption cycles.[24] Unfortunately, $[Ir(tpy)_2]I_3{\cdot}nH_2O$ does not emit luminescence at room temperature, and the vapochromic response is observed through a broad UV-vis absorption spectrum, and therefore the spectral changes were too small to analyze the interaction of the Ir(III) complex with the counter anion involved in vapochromism. In the present work, we prepared an emissive $[Ir(tpy)_2]Br_3{\cdot}7H_2O$ to observe the luminescence vapochromic response at room temperature. The complex crystal shows a reversible luminescence colour change during the sorption/desorption of $H_2O$ molecules, along with a change in crystal structure, which is characteristic of "soft crystals".

# Experimental

### Preparation

$[Ir(tpy)_2]Br_3{\cdot}7H_2O$ was prepared from $[Ir(tpy)_2]I_3{\cdot}2H_2O$[24] by an ion-exchange method. $[Ir(tpy)_2]I_3{\cdot}2H_2O$ (74 mg, 0.071 mmol) and AgBr (53 mg, 0.28 mmol) were dissolved in water and subsequently stirred for 1 day under dark conditions. Removing the white precipitate by filtration afforded a clear yellow solution. After solvent evaporation, the resultant yellow solid material was washed with acetone and acetonitrile; yield 41 mg (67%). A single crystal $[Ir(tpy)_2]Br_3{\cdot}7H_2O$ suitable for X-ray crystal structure analysis was prepared by the slow evaporation of the solvent from an acetonitrile solution containing $[Ir(tpy)_2]Br_3$. Another single crystal $[Ir(tpy)_2]Br_3{\cdot}2H_2O$ suitable for X-ray crystal structure analysis was prepared by the vapor-diffusion method. To a large vial containing an acetone/dimethyl sulfoxide (2 : 1) mixture, as a poor solvent, a small vail containing an acetonitrile solution of $[Ir(tpy)_2]Br_3$ was placed. The large vial was capped and left to stand for 2 weeks, which yielded orange-emissive single crystals.

### Measurements

UV-vis absorption spectroscopy was conducted using a JASCO spectrometer V-530ST. A 1 cm quartz cuvette attached with a grease-less valve was used for UV-vis measurements of a solid sample deposited as a thin-film on the inner wall of the cuvette. The emission spectra were measured by a JASCO FP-6500 spectrofluorometer. The samples for emission measurements were prepared in a quartz cuvette attached with a greaseless valve. The emission lifetimes were evaluated by the least squares method on a PC for time periods of luminescence recorded by a Tektronix TDS1102C digital oscilloscope after pulse excitation using a Japan Laser GL-3300 $N_2$ laser (337 nm). Thermogravimetric (TG) measurements were performed using a Hitachi Hightech Science STA7300. The solid sample stored in an aluminum pan was heated from 293 to 500 K at a heating rate of 5 K $min^{-1}$ under a nitrogen gas atmosphere. Differential scanning calorimetry (DSC) measurements were carried out in the range from room temperature to 400 K using a Hitachi High-Tech Science DSC 7020. Powder X-ray diffraction (PXRD) measurements were performed using a Bruker D8 ADVANCE equipped with a TTK450 for variable temperature measurement. The PXRD patterns for $[Ir(tpy)_2]Br_3{\cdot}7H_2O$, $[Ir(tpy)_2]Br_3{\cdot}2H_2O$, $[Ir(tpy)_2]Br_3{\cdot}H_2O$, and $[Ir(tpy)_2]Br_3$ were measured at 25 °C, 80 °C, 110 °C, and 190 °C, respectively. A PXRD measurement to track the change from $[Ir(tpy)_2]Br_3{\cdot}2H_2O$ to $[Ir(tpy)_2]Br_3{\cdot}7H_2O$ was conducted at room temperature, where $[Ir(tpy)_2]Br_3{\cdot}2H_2O$ was prepared from $[Ir(tpy)_2]Br_3{\cdot}7H_2O$ by the desorption of $5H_2O$ molecules at 80 °C.

### X-ray crystallography

The X-ray diffraction data were obtained at 123 K using a Rigaku XtaLAB Synergy-DW system with MoKα radiation. Indexing, integration, scaling, and absorption correction of the diffraction data were carried out using CrysAlis$^{Pro}$.[33] The structure was solved by the SHELXT 2014 program[34] and refined by full-matrix least-squares techniques against $F^2$ (SHELXL-2019/3)[35] with the Shelxle software package.[36] The non-hydrogen atoms were refined anisotropically. The crystal and molecular structures were drawn using the Mercury software.[37]

# Results and discussion

### $H_2O$ desorption/sorption

A thermogravimetry (TG) measurement was conducted for a $[Ir(tpy)_2]Br_3{\cdot}7H_2O$ (**M7**, tpy = 2,2′:6′,2″-terpyridine) salt prepared by the addition of acetone into an acetonitrile solution containing the Ir(III) complex. As shown in Fig. 1, the TG (black) and DTG (red) results clearly show a three-step weight loss; the peaks of the DTG curve are observed at 60 °C, 90 °C, and 140 °C. For the 1st stage, the weight change reaches −8.80% up to 65 °C, which matches the loss of 5 $H_2O$. A gradual decrease in weight at the initial stage below 50 °C suggests that one $H_2O$ molecule among the water of hydration of **M7** can be easily removed from the crystal framework, which likely occurs even at room temperature. The weight changes in the 2nd and 3rd stages correspond to −1.75% and −1.76%, respectively, each of which is due to the loss of a single $H_2O$ molecule. Since there is no remarkable weight-loss in the region of 65–80 °C, it is reasonably assigned that the crystal heated at 80 °C is $[Ir(tpy)_2]$

 

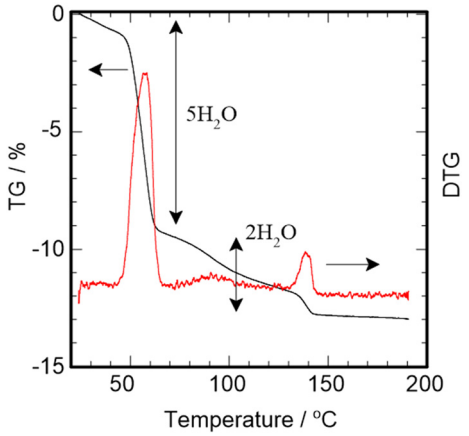


**Fig. 1** TG (black) and DTG (red) plots of $[Ir(tpy)_2]Br_3{\cdot}7H_2O$ (**M7**). Three distinct peaks are observed at 60 °C, 90 °C, and 140 °C in the DTG curve.

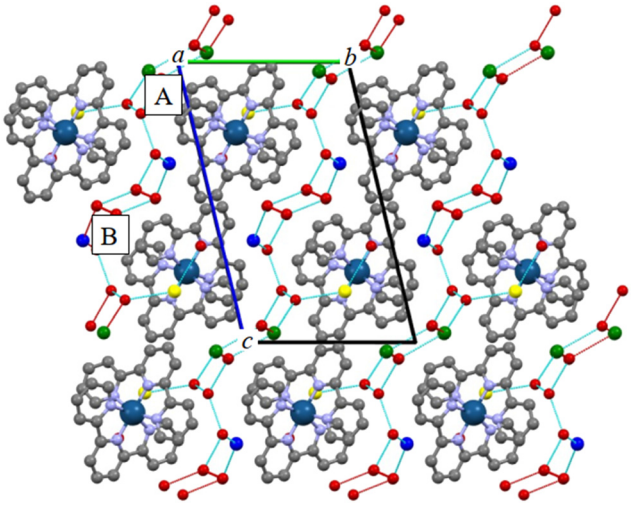


**Fig. 2** Crystal structure of **M7**. **A** and **B** denote the $[Ir(tpy)_2]^{3+}$–$Br^-$ pairs projected on the *bc*-plane when viewed along the *a*-axis. Red circles are O atoms from the water of hydration. The small green, red, and blue circles each represent $Br^-$. The coloured lines between O and Br show the hydrogen bonds. Hydrogen atoms are omitted for clarity.

$Br_3{\cdot}2H_2O$ (**M2**). $[Ir(tpy)_2]Br_3{\cdot}H_2O$ (**M1**) and $[Ir(tpy)_2]Br_3$ (**M0**) are suggested to be obtained by heating at 90–100 °C and 140 °C, respectively. The intermediate phases of **M5–M3** seem not to have been detected through the TG measurement. When **M0** was cooled at room temperature under a humid atmosphere, the weight loss was recovered by the sorption of $H_2O$. Fig. S1 shows the TG results for two samples subjected to the heating–cooling treatment, where the number of water molecules of hydration is determined to be 6.0 and 6.4, respectively. This result suggests that the $H_2O$ sorption from **M0** to **M7** is incomplete at room temperature.

Fig. S2 shows the DSC result of **M7** during heating under an $N_2$ atmosphere. Two distinct endothermic peaks are observed in the range of 30–70 °C and 105–125 °C, which correspond to endothermic processes for the desorption of $5H_2O$ and $2H_2O$, respectively. Since the endothermic amount at 105–125 °C is +13 kJ $mol^{-1}$, we can estimate the endothermic amount of single $H_2O$ desorption to be +6.5 kJ $mol^{-1}$. It is less than the distillation enthalpy of $H_2O$ ($\Delta H$ = +44.016 kJ $mol^{-1}$ at 298 K),[38] suggesting that the elimination of $H_2O$ from **M2** and **M1** easily occurs. In contrast, the endothermic amount of +107 kJ $mol^{-1}$ at 30–70 °C is much larger than the +32.6 kJ $mol^{-1}$ for $5H_2O$ desorption. It is suggested that the transition from **M7** to **M2** needs a large thermal energy for the change in the Ir–$Br^-$ framework in the crystal in addition to the $5H_2O$ desorption.

### Crystal structures of M7 and M2

We determined the crystal structure of **M7** as a triclinic crystal system with the $P\bar{1}$ space-group (Table S1). The X-ray diffraction study on this sample was performed at −150 °C and the number of $H_2O$ molecules was determined to be 7 in the unit cell. When viewed from the *a*-axis of the unit cell, each Ir(III) complex aligns its principal axis of the $D_2$ structure parallel to the *a*-axis, as shown in Fig. 2. Molecules of the water of hydration are accommodated in voids between Ir(III) complexes on the *bc*-plane and form a hydrogen-bond network together with $Br^-$. These hydrogen bonds are expanded along the *a*-axis to construct a 2D sheet structure. Two $Br^-$ ions, coloured with green and blue, are buried in the 2D sheets, while the other ion (yellow) is close to Ir ($l_{Ir1-Br2}$ = 4.729 Å) and is located between two tpy ligands with a bite angle of 78.88° as to be pinched with a scissors of ligands when viewed from the (*b*–*c*)/2 axis of the unit cell (Fig. S3). The Ir–$Br^-$ pair (**A**) and its turnover (**B**) are alternately ordered in a straight line, parallel to the hydrogen bonding networks. The distances between $Br^-$ and O are in the range of 3.285–3.366 Å and those of O–O are at 2.751–2.814 Å (Table S2). An eight-membered ring consisting of $2Br^-$ (Br1) and 6O (O4, O5, O6) is observed in the unit cell. O5 and O6 connect to O5 and O6 in adjacent unit cells, respectively, thereby extending the hydrogen bonding network along the *a*-axis (Fig. S4). O1, O2, O3, and Br3 contribute to the extension of the network along the direction of the (*b*–*c*)/2 axis. Br2 connects to O1 and O7 through hydrogen bonding. It is observed that O7 forms a hydrogen bond with Br2 alone, suggesting the hydrogen bond between Br2 and O7 is weak.

X-ray crystallography analysis determined that the crystal system of **M2** is orthorhombic with the $Pna2_1$ space-group (Table S3). As well as **M7**, two Ir–$Br^-$ pairs (**C** and **D**) are observed in the **M2** crystal, as shown in Fig. 3. Each Ir(III) complex is in an almost perfect $D_{2d}$ symmetry and aligns its principal $C_2$ axis parallel to the *a*-axis of the unit cell. $Br^-$ (yellow) is located on the $C_2$ axis and seems not to form any hydrogen bond with $H_2O$. The closest distance between $Br^-$ and Ir is determined as $l_{Ir1-Br38}$ = 4.640 Å for the Ir–$Br^-$ pair. The pairs **C** and **D** in Fig. 3 are equivalent to each other, yet **D** is the turn-over of **C** with respect to the *bc*-plane and located with an offset of *a*/2 with respect to **C**. The other $Br^-$ ions (green and blue) contribute to hydrogen-bonding with the water of hydration, respectively, to construct 1D channels

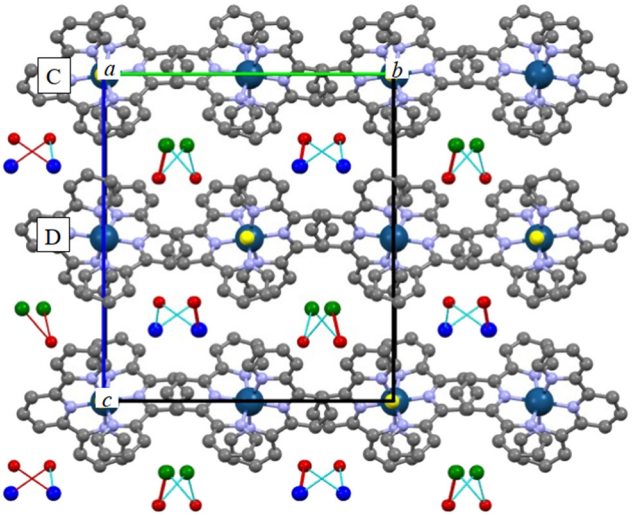


Fig. 3 Crystal structure of **M2**. **C** and **D** denote the $[Ir(tpy)_2]^{3+}$–$Br^-$ pairs projected on the *bc*-plane when viewed along the *a*-axis. Red circles are the O atoms of the water of hydration. The small green, red, and blue circles each represent $Br^-$. The coloured lines between O and Br show the hydrogen bonds. Hydrogen atoms are omitted for clarity.

along the *a*-axis. The distances between O and $Br^-$ are $l_{Br40–O42}$ = 3.358 Å and $l_{Br39–O41}$ = 3.355 Å, respectively (see Table S4 and Fig. S5). The hydrogen bonds are extended along the *a*-axis of the unit cell. In addition, we found a very interesting and rare phenomenon, which is the electron deficiency around $Br^-$ (yellow) with no hydrogen bonding (Fig. S6). Although this might be due to a partial electron transfer from $Br^-$ to the Ir(III) complex, we could not observe any increase in electron density around $[Ir(tpy)_2]^{3+}$. This could be because Ir, as a heavy atom with many electrons, causes any such increase to fall within the experimental error range and thus remain undetected.

The X-ray crystallography for **M7** and **M2** clarified that the difference in the number of water of hydration in the crystal causes the difference in the hydrogen-bond networks. $H_2O$ can be eliminated through the 2D hydrophilic sheet in the desorption process from **M7** to **M2**. The $5H_2O$ loss results in the rearrangement of the Ir–$Br^-$ framework, along with the change in the hydrophilic channel from 2D sheets to 1D columns and with the release of $[Ir(tpy)_2]^{3+}$ from the stress due to the distorted structure. The distortion energy for the $[Ir(tpy)_2]^{3+}$ moiety was predicted through a DFT calculation[39] performed by using CAM-B3LYP as a functional and the basis set of 6-31G* for H, C, N, O, Br, and LANL2DZ for Ir. In this calculation, the geometries for the distorted and undistorted structures were fixed to those of $[Ir(tpy)_2]^{3+}$ from the X-ray crystal structures for **M2** and **M7**, respectively, and $Br^-$ and $H_2O$ were omitted. The relative energy of the distorted structure in **M7** with respect to the $D_{2d}$ structure in **M2** was predicted to be +7.32 kJ $mol^{-1}$. Even though this exothermic energy is consumed for the conversion from **M7** to **M2**, it is too small to compensate for the endothermic energy of +107 kJ $mol^{-1}$ for the phase transition from **M7** to **M2** determined by the DSC measurement.

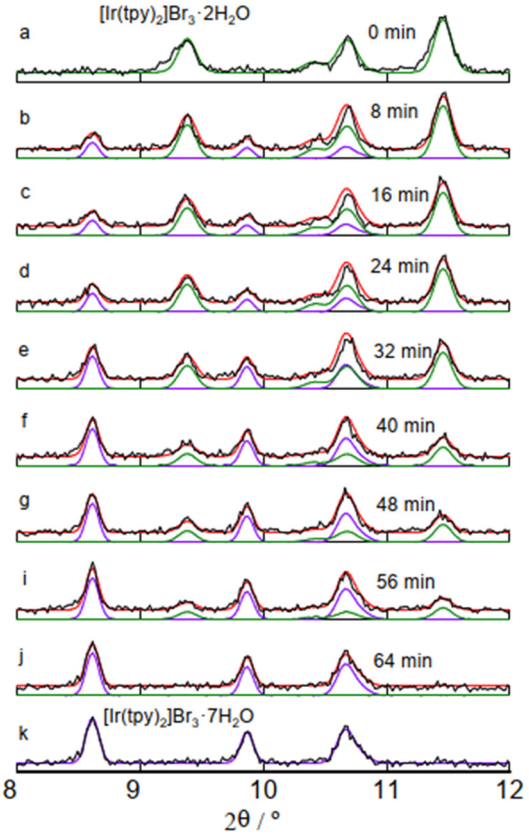


Fig. 4 Variation in the PXRD pattern of **M2** prepared by heating at 80 °C upon cooling to room temperature. The diffraction patterns are observed every 8 min. For **M2** (a) and **M7** (k), each experimental PXRD pattern (black) is reproduced with four Gauss functions, and the resultant simulations are displayed as green and purple, respectively. The red curves (b–i) superimposed by the simulations for **M2** (green) and **M7** (purple) are the best fit to the PXRD patterns (c–k, black), respectively.

### Rearrangement of the Ir–$Br^-$ framework

To detect the Ir–$Br^-$ framework change experimentally, the $H_2O$ sorption process for **M2** was tracked through the PXRD measurement, where the diffraction pattern at $2\theta$ = 8–12° for **M2** prepared by heating at 80 °C was recorded every 8 min to observe the change in peaks during the sorption of $H_2O$ molecules by cooling. As shown in Fig. 4, three distinct peaks at $2\theta$ = 9.4°, 10.7°, 11.5° and a small peak at $2\theta$ = 10.4° are observed initially (a, black), consistent with the powder pattern simulated from the result of the single crystal X-ray diffraction. The peaks at 9.4°, 10.4°, and 11.5° gradually become small and disappear in 64 min, as displayed in (b)–(j). Instead, new peaks emerge at 8.6° and 9.9° and grow larger over time. Eventually, three peaks at $2\theta$ = 8.6°, 9.9°, and 10.7° remain in the powder pattern (j). The peak shape at 10.7° appears asymmetric due to the shoulder at the higher angle. These peaks are consistent with the PXRD pattern for **M7** (k). Clearly, the change in diffraction pattern corresponds to the change in the Ir–$Br^-$ framework in the crystal during the $H_2O$ sorption process from **M2** to **M7**.

Despite the fact that this $H_2O$-sorption process took around 60 min for completion, no apparent peaks for **M3–M6** were detected. This suggests that (1) the $H_2O$ sorption is too rapid to detect the peaks for **M3–M6** by our apparatus, (2) the crystal systems of **M3–M6** are the same as that of **M7** or **M2**, or (3) **M3–M6** are not detected by PXRD because of the lack of crystallinity. In the case of (1), considering that the **M2** used is a powdery sample consisting of many fine crystals, the slow change in peak intensity might be due to the statistical change of the **M2** content in the entire fine crystals, where the rapid $H_2O$ sorption of each fine crystal occurs. In that case, any PXRD pattern should be the superposition of those of **M2** and **M7**. In the case of (2), the crystal systems of **M3–M6** are expected to be the same as that of **M7**. Since there is no void space in the **M2** crystal to accommodate extra $H_2O$ molecules, if $H_2O$ molecules are forced to insert into the **M2** crystal, the Ir–$Br^-$ framework of **M2** will change to that of **M7** to accommodate extra $H_2O$ molecules. Considering that the X-ray diffraction intensity is proportional to the number of electrons, the XRD peak intensities for **M3–M7** may be varied by the number of $H_2O$ molecules, even though the peaks are observed at the same $2\theta$ angles (Fig. S7). The observed PXRD patterns during the $H_2O$ sorption will not be reproduced from the simple superposition of those of **M2** and **M7**. Regarding case (3), the lack of crystallinity might be provided by a variety of structural changes in the Ir–$Br^-$ framework due to the squeezing of extra $H_2O$ molecules into the **M2** crystal. In this case, the transient domains of **M3–M6** would contribute to the depletion of the PXRD intensity.

In Fig. 4, simulations of the PXRD patterns are exhibited as coloured curves. The patterns of **M2** (a) and **M7** (k) were reproduced using four Gauss functions and displayed as green and purple curves, respectively. For (b)–(j), the patterns simulated by the superposition of green and purple curves are displayed as red curves, respectively, which sufficiently match each experimental result. This concludes that the intermediate phases are not detected in the present work; that is, the $H_2O$ sorption process along with the framework change is too rapid to detect though the PXRD measurement. Fig. S8 shows plots of the composition of **M2** and **M7** in the simulation, where the change in composition is shown to be neither linear nor exponential but stepwise. This result might suggest some difference in the rate of framework change depending on the inhomogeneity in the crystal size of **M2**.

### Structure of M1 and M0

The PXRD measurements were carried out for $[Ir(tpy)_2]Br_3{\cdot}7H_2O$ at 190, 110, 75, and 25 °C, respectively. The results are exhibited as red lines in Fig. S9, where we assigned the samples at 190, 110, 75, and 25 °C to **M0**, **M1**, **M2**, and **M7**, respectively, according to the TG results. The blue line of **M7** is derived from a simulation of the single crystal X-ray diffraction analysis, which is in good agreement with the experimental pattern at 25 °C. For **M2**, as well, the pattern observed at 75 °C is very similar to the simulation from the single crystal X-ray diffraction result, suggesting the crystal structure of the Ir(III) complex prepared by heating at 75 °C from **M7** is the same as that of **M2** directly prepared by crystallization from the acetonitrile solution. This indicates that the dehydration processes from **M7** to **M2** are a single-crystal to single-crystal transition. Considering $V$ = 1750.47 Å$^3$ for **M7** ($Z$ = 2) and $V$ = 2963.01 Å$^3$ for **M2** ($Z$ = 4) from the single crystal X-ray analyses, the net difference in volume is roughly estimated as 134 Å$^3$ when converted into the case of $Z$ = 1. It should be noted that this volume difference is comparable to 150 Å$^3$, the sum of volumes of $5H_2O$. Both the patterns of **M1** and **M0** coincide with that of **M2**, which suggests that their packing structures consisting of $[Ir(tpy)_2]^{3+}$ and $3Br^-$ are very similar to one another; that is, the crystal frameworks are robust and retain the same structure during $H_2O$ desorption by heating. This result suggests that the dehydration processes from **M2** to **M1** to **M0** are single-crystal to single-crystal transitions. The temperature effect on peak angles is recognized; for example, the peaks at the lowest angle are observed at 9.337° (**M2**), 9.408° (**M1**), and 9.428° (**M0**). The variation in peak angles would be due to the combination of the thermal expansion of the crystal lattice and the contraction resulting from the elimination of $H_2O$. Rietveld analyses[40] of the PXRD patterns were performed for **M2**, **M1** and **M0**, where the geometry of the Ir(III) complex and the space group are the same as those in **M2** determined by the single crystal X-ray structural analysis. Results are in good agreement with the experimental patterns (Fig. S9). As listed in Table S5, although the lattice parameters $a$, $b$, and $c$ decrease slightly or remain the same with increasing temperature, the volumes clearly decrease. The decrease in volume from **M2** to **M0** is 14.8 Å$^3$, which is very small, considering the volume of a single $H_2O$ molecule is 30 Å$^3$ and $Z$ = 4 in the $Pna2_1$ space group. The small change in volume might guarantee the robustness of the crystal framework during the sorption/desorption of $H_2O$.

### Vapochromic behaviour

As shown in Fig. 5, **M7** emits yellow luminescence showing vibronic structure peaks at 507, 544, and 581 nm, which can be assigned to the π–π* transition of the ligand.[32] Upon heating at 80 °C for 5 min, surprisingly, the yellow luminescence changes to orange resulting in a broad spectrum centered at 623 nm. This broad emission is likely due to the $Br^-$-to-ligand charge transfer (XLCT) transition of **M2**, according to the emission study on $[Ir(tpy)_2]_2X_3$ ($X^-$ = $Cl^-$, $Br^-$, and $I^-$) at 77 K.[32] The luminescence colour returns to original yellow in 40 min when the crystalline sample is cooled under ambient atmosphere. Since the luminescence change is more sensitive than the colour change, the $[Ir(tpy)_2]Br_3$ crystal showing the visible luminescence vapochromism is superior to the non-emissive $[Ir(tpy)_2]I_3$ system previously reported.[32] We note that the emission profile of **M7** appears to be a superposition of the structured π–π* emission and the broad XLCT emission. This

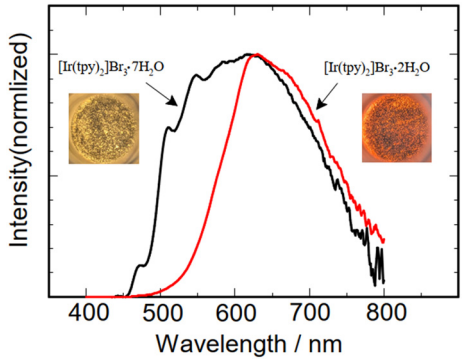


**Fig. 5** Photographs (insets) and emission spectra of the $[Ir(tpy)_2]Br_3{\cdot}7H_2O$ (**M7**) and $[Ir(tpy)_2]Br_3{\cdot}2H_2O$ (**M2**) crystals observed at room temperature.

spectrum is similar to that of the dual emission of $[Ir(tpy)_2](PF_6)_3$ in acetonitrile,[32] where structured and broad emissions were assigned to the individual emissions of $[Ir(tpy)_2]^{3+}$ and $[Ir(tpy)_3]^{3+}{\cdot}PF_6^-$, respectively, in the ion-association equilibrium. As well, in the present case, the broad emission component of **M7** is probably assigned to the XLCT emission of the $[Ir(tpy)_3]^{3+}{\cdot}Br^-$ pair, in which the $Br^-$ bearing $H_2O$ is located on the pseudo $C_2$ axis of the Ir(III) complex with $l_{Ir1-Br2}$ = 4.729 Å. The broad emission of **M7** is blue shifted, along with sharpening at 77 K, as shown in Fig. S10, which is a familiar phenomenon for the CT emissions of metal complexes. On the other hand, the structured emission at around 500 nm attributable to the π–π* emission remains even at 77 K. These results support that the emission of **M7** is assigned to the dual emission.

An emission lifetime measurement was conducted for **M7** and **M2** at room temperature. The time course of the **M7** emission monitored at 500 nm, a peak wavelength of the vibronic band of the π–π* emission, consists of fast and slow decay curves (Fig. S11a); the lifetimes of the fast and slow components are estimated to be 20 ns and 300 ns, respectively, by a least square fitting using a double exponential function. When monitored at 650 nm, the peak wavelength of the broad emission, the emission lifetime was determined as $\tau$ = 540 ns, which is longer than $\tau$ = 300 ns. The longer the monitoring wavelength, the longer the emission lifetime. On the other hand, the emission lifetime of **M2** monitored at 650 nm is determined as $\tau$ = 860 ns (Fig. S11b). $H_2O$ desorption likely elongates the XLCT emission lifetime, probably because of the prevention from nonradiative deactivation due to the O–H vibration of $H_2O$. Consequently, the luminescence vapochromism of **M7** is established to originate from switching of the emitting state from the π–π* state to the XLCT state, probably due to the proximity of $Br^-$ and $[Ir(tpy)_2]^{3+}$.

This luminescence-colour conversion is repeatedly observed, as shown in Fig. S12, which are plotted as the emission intensities of the sample at 540 nm upon heating (red) for 10 min and cooling (black) for 20 min under a humid atmosphere alternately. Although the emission intensities of the heated sample are stable during the heating–cooling cycles, those after cooling seem to vary. Fig. S13 shows a change in the emission spectra of the heated sample (**M2**) observed at room temperature under a humid atmosphere. The broad band at 610 nm gradually decreases in intensity, along with the growth of vibronic bands in the region of 500–550 nm. The iso-emissive point observed at 570 nm at the initial stage eventually disappears. By analogy to the TG results, it is suggested that **M2** is not converted to **M7** completely upon cooling but to the **M7**/**M6** mixture.

Although we cannot perceive the remarkable colour difference in the luminescence of **M2**–**M0**, the emission spectrum of **M2** slightly shifted to the longer wavelength region upon removing $H_2O$ from the crystal by heating. The resultant spectra of **M1** and **M0** are similar to each other, as shown in Fig. S14. The UV absorption spectrum in the 250–400 nm region of **M2** is also shifted to the longer wavelength region by heating to produce **M1** and **M0**. This phenomenon is very similar to that found for the $[Ir(tpy)_2]I_3{\cdot}2H_2O$–$[Ir(tpy)_2]I_3$ system previously, where the reversible colour change between yellow and orange due to the sorption/desorption of $2H_2O$ is observed.

## Conclusion

We found the vapochromism due to the reversible $H_2O$ sorption/desorption for the cationic complex crystal $[Ir(tpy)_2]Br_3{\cdot}nH_2O$ ($n$ = 7–0). The X-ray crystallography revealed the hydrophilic 2D sheets and channels in $[Ir(tpy)_2]Br_3{\cdot}7H_2O$ (triclinic) and $[Ir(tpy)_2]Br_3{\cdot}2H_2O$ (orthorhombic), respectively, both consisting of $H_2O$ and $Br^-$ interacting *via* hydrogen bonding. The heating of the yellow $[Ir(tpy)_2]Br_3{\cdot}7H_2O$ crystal results in the removal of $H_2O$ molecules hydrated to $Br^-$, followed by the orange colouration due to the emergence of the XLCT absorption band in the visible region. This vapochromic process is accompanied by the drastic change in the Ir–$Br^-$ framework in the crystal, which is a characteristic behaviour for "soft crystals" and a novel phenomenon for cationic transition metal complexes. For $[Ir(tpy)_2]Br_3{\cdot}2H_2O$, the rigidity of the Ir–$Br^-$ framework makes it possible for the $H_2O$ desorption process producing empty channels, whereas flexibility is necessary to insert $H_2O$ molecules into the occupied channels. It is notable that a weak stimulus, such as exposure to moisture, causes a drastic change in the crystal from triclinic to orthorhombic. Unfortunately, analysis of the mechanism of the dynamic structural change from triclinic to orthorhombic was not achieved through the detection of intermediate phases for $[Ir(tpy)_2]Br_3{\cdot}nH_2O$ ($n$ = 6–3) in the present work. If successful, it would greatly contribute to our scientific understanding of "Soft Crystals," changing crystal structure upon weak external stimulus. $[Ir(tpy)_2]Br_3{\cdot}7H_2O$ was found to emit the dual emission from the π–π* and XLCT states depending on the strength of interaction between the Ir(III) complex and $Br^-$. The heating of $[Ir(tpy)_2]Br_3{\cdot}7H_2O$ contributes to not only the framework change but also the detachment of $H_2O$ from the hydrated $Br^-$. Thereby, the interaction between the Ir(III) complex and $Br^-$ is strong and stabilizes the XLCT state in

 

energy, resulting in the quenching of the π–π* emission. The switching of the excited state between the π–π* and XLCT states is one of the valuable findings in the present work.

## Conflicts of interest

There are no conflicts to declare.

## Data availability

The data supporting this article have been included as part of the supplementary information (SI).

Supplementary information: crystallographic data and additional figures and tables. See DOI: https://doi.org/10.1039/d6ce00194g.

CCDC 2527091 ([Ir(tpy)$_2$]Br$_3$·7H$_2$O) and 2527097 ([Ir(tpy)$_2$]Br$_3$·2H$_2$O) contain the supplementary crystallographic data for this paper.[41a,b]

## Acknowledgements

We thank the Institute of Science Tokyo Core Facility Center for the provision of the dual wavelength single-crystal X-ray diffractometer (Rigaku XtaLAB Synergy-DW system). This work was supported by JSPS KAKENHI (grant number JP21K14647).

## References

1 T. Abe, T. Itakura, N. Ikeda and K. Shinozaki, Luminescence color change of a platinum(II) complex solid upon mechanical grinding, *Dalton Trans.*, 2009, 711–715.
2 Y. Nishiuchi, A. Takayama, T. Suzuki and K. Shinozaki, A Polymorphic Platinum(II) Complex: Yellow, Red and Green Polymorphs and X-ray Crystallography of [Pt(fdpb)Cl] (Hfdpb = 1,3-Di(5-trifluoromethyl-2-pyridyl)benzene), *Eur. J. Inorg. Chem.*, 2011, **2011**, 1815–1823.
3 J. Ni, X. Zhang, N. Qiu, Y.-H. Wu, L.-Y. Zhang, J. Zhang and Z.-N. Chen, *Inorg. Chem.*, 2011, **50**, 9090–9096.
4 X.-P. Zhang, J.-F. Mei, J.-C. Lai, C.-H. Li and X.-Z. You, *J. Mater. Chem. C*, 2015, **3**, 2350–2357.
5 Y. Shigeta, A. Kobayashi, M. Yoshida and M. Kato, *Cryst. Growth Des.*, 2018, **18**, 3419–3427.
6 M. Martinez-Junquera, R. Lara, E. Lalinde and M. T. Moreno, *J. Mater. Chem. C*, 2020, **8**, 7221–7233.
7 C.-Y. Lien, Y.-F. Hsu, Y.-H. Liu, S.-M. Peng, T. Shinmyozu and J.-S. Yang, *Inorg. Chem.*, 2020, **59**, 11584–11594.
8 Y. Yin, Z. Chen, R.-H. Li, C. Yuan, T.-Y. Shao, K. Wang, H. Tan and Y. Sun, *Inorg. Chem.*, 2021, **60**, 9387–9393.
9 M. Martínez-Junquera, E. Lalinde and M. T. Moreno, *Inorg. Chem.*, 2022, **61**, 10898–10914.
10 Y. Shigeta, T. Nomoto, M. Kato and M. Mizuno, *Inorg. Chem.*, 2023, **62**, 66–74.
11 H.-H. Zhang, S.-X. Wu, Y.-Q. Wang, T.-G. Xie, S.-S. Sun, Y.-L. Liu, L.-Z. Han and X.-P. Z.-F. Shi, *Dyes Pigm.*, 2022, **197**, 109857.
12 M. Cocchi, J. Kalinowski, V. Fattori, J. A. G. Williams and L. Murphy, *Appl. Phys. Lett.*, 2009, **94**, 073309.
13 S. J. Farley, D. L. Rochester, A. L. Thompson, J. A. K. Howard and J. A. G. Williams, *Inorg. Chem.*, 2005, **44**, 9690–9703.
14 S. Develay, O. Blackburn, A. L. Thompson and J. A. G. Williams, *Inorg. Chem.*, 2008, **47**, 11129–11142.
15 M. Cocchi, D. Virgili, V. Fattori, D. L. Rochester and J. A. G. Williams, *Adv. Funct. Mater.*, 2007, **17**, 285–289.
16 W. Mróz, C. Botta, U. Giovanella, E. Rossi, A. Colombo, C. Dragonetti, D. Roberto, R. Ugo, A. Valore and J. A. G. Williams, *J. Mater. Chem.*, 2011, **21**, 8653–8661.
17 M. Cocchi, J. Kalinowski, V. Fattori, J. A. G. Williams and L. Murphy, *Appl. Phys. Lett.*, 2009, **94**, 073309.
18 N. M. Barker, S. D. Taylor, E. Ferguson, J. A. Krause, A. G. Oliver, W. B. Connick and P. Zhang, *Inorg. Chem.*, 2021, **60**, 14731–14743.
19 C. L. Stubbs, M. J. Bryant, L. E. Hatcher and P. R. Raithby, *CrystEngComm*, 2025, **27**, 7498–7513.
20 Y. Li, L. Chen, Y. Ai, E. Y.-H. Hong, A. K.-W. Chan and V. W.-W. Yam, *J. Am. Chem. Soc.*, 2017, **139**, 13858–13866.
21 S. Hattori, T. Nakano, N. Kobayashi, Y. Konno, E. Nishibori, T. Galica and K. Shinozaki, *Dalton Trans.*, 2022, **51**, 15830–15841.
22 M. Kato and K. Ishii, *Soft Crystals: Flexible Response Systems with High Structural Order (The Materials Research Society Series)*, Springer, 2023.
23 M. Kato, H. Ito, M. Hasegawa and K. Ishii, *Chem. – Eur. J.*, 2019, **25**, 5105–5112.
24 S. Hattori, M. Kondo, A. Sekine and K. Shinozaki, Vapochromism of an iridium(III) bis-terpyridine complex based on the modulation of halide-to-ligand charge transfer transition, *Dalton Trans.*, 2022, **51**, 7068–7075.
25 P. Alam, M. Karanam, D. Bandyopadhyay, A. R. Choudhury and I. R. Laskar, *Eur. J. Inorg. Chem.*, 2014, 3710–3719.
26 P. Alam, M. Karanam, D. Bandyopadhyay, A. R. Choudhury and I. R. Laskar, *Eur. J. Inorg. Chem.*, 2014, 3710–3719.
27 E. V. Nykhrikova, M. A. Kiseleva, P. Kalle, S. S. Mariasina, S. A. Kozyukhin, S. V. Tatarin and S. I. Bezzubov, *Inorg. Chem.*, 2025, **64**, 5210–5220.
28 X. Zhu, P. Cui, S. Kilina and W. Sun, *Inorg. Chem.*, 2017, **56**, 13715–13731.
29 P. Bolle, H. Serier-Brault, R. Génois, E. Faulques, A. Boulmier, O. Oms, M. Lepeltier, J. Marrot, A. Dolbecq, P. Mialane and R. Dessapt, *J. Mater. Chem. C*, 2016, **4**, 11392–11395.
30 Y. Jiang, G. Li, D. Zhu, Z. Su and M. R. Bryce, *J. Mater. Chem. C*, 2017, **5**, 12189–12193.
31 Y. Wang, T. Yang, X. Liu, G. Li, W. Che, D. Zhu and Z. Su, *J. Mater. Chem. C*, 2018, **6**, 12217–12223.
32 W. Ito, S. Hattori, M. Kondo, H. Sakagami, O. Kobayashi, T. Ishimoto and K. Shinozaki, Dual Emission from an Iridium(III) Complex/Counter Anion Ion Pair, *Dalton Trans.*, 2021, **50**, 1887–1894.
33 *CrysAlisPro*, Agilent Technologies Ltd, Yarnton, Oxfordshire, England, 2014.
34 G. M. Sheldrick, SHELXT – Integrated space-group and crystal-structure determination, *Acta Crystallogr., Sect. A: Found. Adv.*, 2015, **71**, 3–8.

35 G. M. Sheldrick, Crystal structure refinement with SHELXL, *Acta Crystallogr., Sect. C: Struct. Chem.*, 2015, **71**, 3–8.
36 C. B. Hübschle, G. M. Sheldrick and B. Dittrich, ShelXle: a Qt graphical user interface for SHELXL, *J. Appl. Crystallogr.*, 2011, **44**, 1281–1284.
37 C. F. Macrae, P. R. Edgington, P. McCabe, E. Pidcock, G. P. Shields, R. Taylor, M. Towler and J. van de Streek, Mercury: visualization and analysis of crystal structures, *J. Appl. Crystallogr.*, 2006, **39**, 453–457.
38 P. Atkins and J. de Paula, *Atkins' Physical Chemistry*, Oxford New York, 9th edn, 2010.
39 M. J. Frisch, G. W. Trucks, H. B. Schlegel, G. E. Scuseria, M. A. Robb, J. R. Cheeseman, G. Scalmani, V. Barone, G. A. Petersson, H. Nakatsuji, X. Li, M. Caricato, A. V. Marenich, J. Bloino, B. G. Janesko, R. Gomperts, B. Mennucci, H. P. Hratchian, J. V. Ortiz, A. F. Izmaylov, J. L. Sonnenberg, D. Williams-Young, F. Ding, F. Lipparini, F. Egidi, J. Goings, B. Peng, A. Petrone, T. Henderson, D. Ranasinghe, V. G. Zakrzewski, J. Gao, N. Rega, G. Zheng, W. Liang, M. Hada, M. Ehara, K. Toyota, R. Fukuda, J. Hasegawa, M. Ishida, T. Nakajima, Y. Honda, O. Kitao, H. Nakai, T. Vreven, K. Throssell, J. A. Montgomery Jr., J. E. Peralta, F. Ogliaro, M. J. Bearpark, J. J. Heyd, E. N. Brothers, K. N. Kudin, V. N. Staroverov, T. A. Keith, R. Kobayashi, J. Normand, K. Raghavachari, A. P. Rendell, J. C. Burant, S. S. Iyengar, J. Tomasi, M. Cossi, J. M. Millam, M. Klene, C. Adamo, R. Cammi, J. W. Ochterski, R. L. Martin, K. Morokuma, O. Farkas, J. B. Foresman and D. J. Fox, *Gaussian 16, Revision C.01*, Gaussian, Inc., Wallingford CT, 2016.
40 F. Izumi and K. Momma, *Solid State Phenom.*, 2007, **130**, 15–20.
41 (*a*) CCDC 2527091: Experimental Crystal Structure Determination, 2025, DOI: 10.5517/ccdc.csd.cc2qtn29; (*b*) CCDC 2527097: Experimental Crystal Structure Determination, 2025, DOI: 10.5517/ccdc.csd.cc2qtn8h.